

Atomistic analysis of Li migration in $\text{Li}_{1+x}\text{Al}_x\text{Ti}_{2-x}(\text{PO}_4)_3$ (LATP) solid electrolytes

Daniel Pfalzgraf, Daniel Mutter* and Daniel F. Urban

Fraunhofer IWM, Wöhlerstr. 11, 79108 Freiburg, Germany

*Author to whom correspondence should be addressed

E-mail: daniel.mutter@iwm.fraunhofer.de

Abstract. We examine the ionic migration of Li in LATP [$\text{Li}_{1+x}\text{Al}_x\text{Ti}_{2-x}(\text{PO}_4)_3$] solid electrolytes from an atomistic viewpoint by means of density functional theory calculations. We vary the Al content and investigate its effects on the crystal structure of LATP and on the migration energy landscape of interstitial Li ions. The energy profiles governing the Li diffusion are found to be systematically influenced by the position of Al ions in direct vicinity of the migration path, and we derive a simplified classification scheme of three universal energy profile shapes. The overall influence of the Al/Ti-ratio on the Li migration is analyzed by a separation into chemical and geometrical aspects. This work provides a solid basis for a resource-efficient computational examination of the ionic conductivity of Li in LATP with varying Al/Ti concentrations.

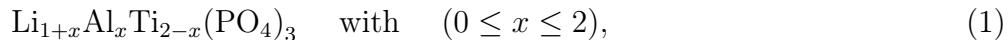
Keywords: ionic migration, diffusion, solid electrolyte, NASICON, LATP

1. Introduction

Modern society is currently facing rapid developments regarding its energetic needs. The importance of energy storage solutions is ever-growing, both in production, with the focus on renewable energy sources, and in consumption, where electronic miniaturization demands novel technologies. For hand-held electronics, the introduction of Li-ion batteries, which generally contain liquid electrolytes (LEs), has been revolutionary. Yet, intrinsic problems hamper the improvement of this technology, such as chemical instabilities at the LE/electrode interfaces at high voltages, or the growth of Li dendrites, which can cause short-circuits [1].

Batteries using solid state electrolytes (SSEs) are regarded as a promising alternative circumventing these issues. Most solids show ionic conductivities which are many orders of magnitude lower than those of state-of-the-art LEs, apparently making SSEs a naturally bad choice for electrolytes. However, some materials exhibit so-called super-ionic conductivity, which elevates them to the same level as LEs regarding their diffusive properties. In addition, SSEs exploit many natural advantages of a solid, such as mechanical stability, which largely suppresses dendrite growth [2, 3, 4].

In this research, we examine the compound class of Lithium Aluminium Titanium Phosphates (LATP),



which has been investigated for its ionic conduction properties since the late 1980s [5]. LATP has seen an increased research interest in recent years, both in simulation and experiment.

As compiled by Rossbach *et al.* [6], LATP is a superionic conductor for certain compositions ($0.2 \leq x \leq 0.5$). This is partially attributed to a growing number of mobile charge carriers with increasing x : In LATP, when substituting tetravalent Ti(4+) by trivalent Al(3+), additional mobile Li(1+) ions are introduced due to charge compensation. However, the increase in ionic conductivity due to the introduced charge carriers was found to be diminished by other factors at values of $x > 0.5$. Furthermore, it was found experimentally that the quality of ionic conduction in LATP is highly dependent on the method of synthesis [7]. The reason for these peculiarities is subject of active research.

The diffusion pathways of Li in LATP are well-investigated [8, 9, 10, 11]. Two different migration mechanisms have been analyzed by atomistic simulations: a vacancy mechanism involving one Li ion, and an interstitial mechanism involving the correlated movement of three Li ions. Experimental data and various atomistic simulations suggest that the interstitial process dominates the superionic conduction in LATP and related compounds [12, 13, 14, 15, 16].

In this study, we apply density functional theory (DFT) calculations to systematically investigate the effect of Al on the interstitial migration process of Li in LATP. In particular, we consider three different aspects: (i) the variation of the structural parameters as function of the Al content, (ii) the influence of a specific local

Al neighborhood on the Li migration barriers and energy profiles, (iii) the dependence of these profiles on the cell volume as determined by the averaged global Al/Ti concentration.

The paper is organized as follows. In [Section 2.1](#), we give a description of relevant LATP properties: Migration pathways of Li are introduced, and general implications of substituting Ti by Al are sketched. In [Section 2.2](#), we describe the computational methods used to generate the data. The data and its direct implications are presented in [Section 3](#), divided into three parts corresponding to the investigated aspects: The first part ([Section 3.1](#)) presents the structural data as a function of Al content. In addition, the dependence of the formation energy of the interstitial Li configuration on the distance to the closest Al ion is examined. The second part ([Section 3.2](#)) focuses on the energy profiles of the interstitial migration mechanism by investigating their dependence on the local Al/Ti neighborhood. In the third part ([Section 3.3](#)), we evaluate the dependence of the migration energy profiles on the volume of the crystal, in order to decouple geometrical from chemical effects, and to determine the influence of the global Al content. The results are discussed in [Section 4](#), and [Section 5](#) summarizes the gained insights and gives an outlook on further research directions.

2. Methods and Model

2.1. Structure of LATP

LATP is a structural derivate of Sodium Zirconium Phosphate (NZP), first described by Hagman and coworkers [17], which belongs to a family of superionic conductors commonly referred to as NASICON. NZP crystallizes in a rhombohedral lattice of space group $R\bar{3}c$. Its characteristic structure of oxygen polyhedra, arranged in so-called “lantern” substructures, stabilizes a three-dimensional network of migration channels suitable for small cations. These structural characteristics of NZP are present in LATP as well. More structural details were described extensively in previous papers (e.g. [12, 18]). Therefore this section mainly focuses on a description of the migration channels and the migration mechanisms of Li.

For our simulations, we choose a hexagonal unit cell as depicted in the top panel of [Figure 1](#). It contains 6 lantern units of stoichiometry $\text{Al}_x\text{Ti}_{2-x}(\text{PO}_4)_3$, two of which are highlighted on the right side of the figure. Interlinked lanterns form a rigid structure, encompassing connected cavities through which Li ions can migrate. As visualized by the balls-and-sticks framework in the top panel of [Figure 1](#), there exist certain discrete positions of Li ions being especially relevant for the diffusion processes, as described in the following.

2.1.1. Li sites In LATP, there are three known symmetry positions of Li ions along the migration channels with special importance to the migration. They are shown in [Figure 1](#) (bottom panel): On the “M1” position (Wyckoff site $6b$, colored green in the

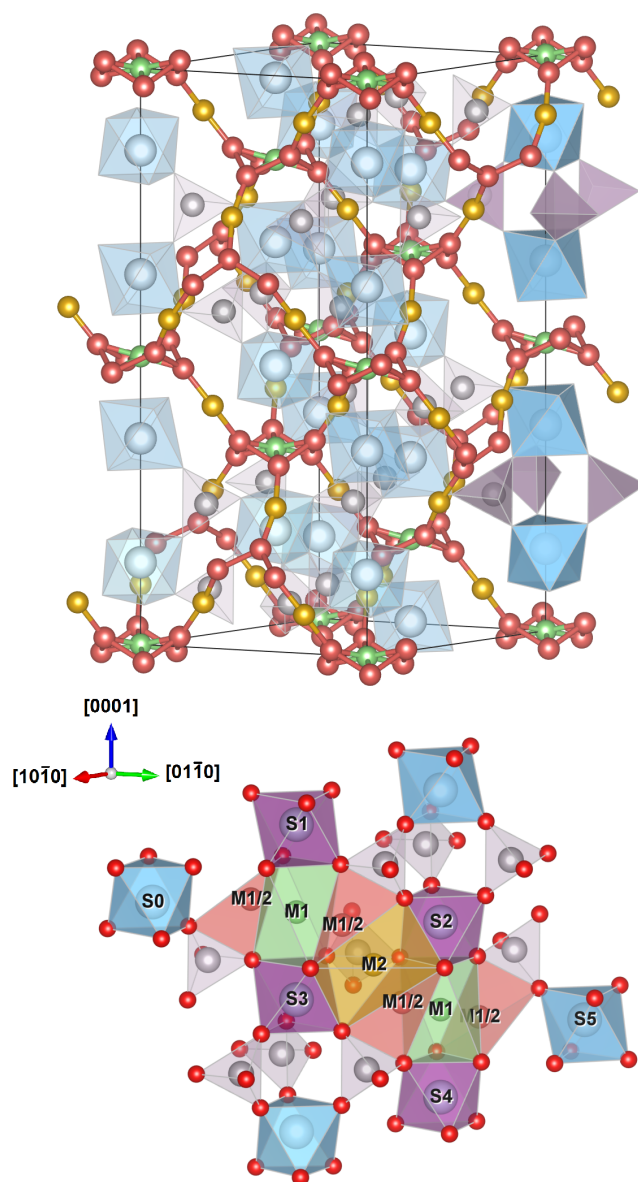


Figure 1. (Color online) Crystal structure of LATP. Top panel: hexagonal unit cell (enclosed by solid lines) with a schematic representation of the migration channels of Li ions. Light blue spheres represent sites occupied by Ti or Al ions, light grey spheres represent P ions. The corners of the octahedra surrounding the sites of Ti and Al, and the tetrahedra surrounding P sites are occupied by O ions (not shown). Green, red brown, and yellow spheres connected by rods represent the M1, M1/2, and M2 sites of Li, respectively, as introduced in [Section 2.1](#). Two characteristic “lantern” substructures, each consisting of two Al/Ti-octahedra (light blue) linked by three P-tetrahedra (light grey), are highlighted on the right. Bottom panel: detailed surroundings of a Li migration pathway. Oxygen ions are represented by red spheres. The labels S0–S5 denote specific sites of Al/Ti occupation (*cf.* [Section 3.2](#)). Polyhedra colored purple highlight the sites (S1, S2, S3, S4) for which occupations were varied in the calculations presented in [Section 3.2](#).

figure), the Li ion sits in between two neighboring lanterns along the [0001] direction. In LTP ($x = 0$, i.e. no Al ions in the structure), the occupation of M1 corresponds to the lowest energy of Li in the structure, meaning that in the ground-state, all M1 sites are occupied. The “M2” site (Wyckoff 18e, orange) is centered halfway in between two such M1 positions. The Li migration mechanism in LATP occurs along this pathway defined by the M1 and M2 sites.

When there are more Li ions in a cell than there are M1 sites, it is observed that an M1 site becomes vacant [6]. DFT calculations show, that this occurs in favor of the occupation of two interstitial “M1/2” sites (Wyckoff 36f, colored red brown in Figure 1) in close proximity to the vacancy [12]. For each M1 site, there are six possible M1/2 sites, arranged around M1 at slight tilt angles with respect to the (0001) plane, in a three-fold rotation symmetry (*cf.* Figure 1). The occupation of two M1/2 sites directly opposite to each other with Li forms a stable M1/2 pair configuration.

Note that the sites are not named consistently in the literature: In this paper, we use the notation and terminology of Lang *et al.* [12].

2.1.2. Migration mechanisms For low Li densities within the structural network, the main migration process for Li is a *vacancy mechanism* involving two M1 sites and their intermediary M2 site: A Li ion occupying an M1 site relocates to a neighboring vacant one, with an M2 occupation as a transition state. This mechanism has been thoroughly examined via DFT calculations and was found to have a migration barrier of $\Delta E \approx 0.41$ eV in the case of LTP [12].

At higher Li densities, the *interstitial mechanism* involving M1/2 pair occupations becomes relevant. In this case, a pair occupation relocates to a neighboring singly-occupied M1 site along the M2 site connecting them. One Li of the former pair then fully occupies the previously vacant M1 site, and the other forms a new M1/2 pair with the previously unpaired ion. In analogy to the vacancy process, we define the M2 transition state as the intermediate step of this process, where both M1 sites and the M2 site in between are occupied by one Li ion each. In LTP, this coincides with the energetic saddle point.

From DFT simulations, the energy barrier $\Delta E \approx 0.19$ eV of the interstitial mechanism in LTP was found to be considerably lower than that of the vacancy mechanism [12]. However, this migration process results in an effectively reduced dimensionality of the network: The Li M1/2 pairs have a fixed orientation along which the migration process can occur, and transitions between the three possible orientations are suppressed by an additional energy barrier of the same order as that of the migration step itself [12]. Still, the interstitial process is expected to be the main reason for the super-ionic conductivity of LATP [13, 14].

2.1.3. Substitution of Ti by Al Due to its significantly lower barriers, the interstitial process could be facilitated when designing a superionic conductor based on the NZP structure, since the ionic conductivity scales as an inverse exponential of the migration

barrier (Arrhenius equation). In LATP, as mentioned earlier, this can be achieved by increased substitution of Ti(4+) by Al(3+). The Al ion replaces a Ti ion on its site, leaving the general structure unchanged. An additional Li ion is required for maintaining charge neutrality, leading to an increase of the parameter x (*cf.* Equation (1)). As the additional Li ions form M1/2 pairs with former M1 site ions, the interstitial process is expected to gain importance. Experimentally, however, the benefits of this substitution to the ionic conductivity are limited: While the conductivity improves with increasing x up to $x \approx 0.5$, a decrease of both total and bulk ionic conductivity is observed for higher values of x [5, 8]. This decrease in total conductivity might be caused by grain boundaries and the formation of secondary phases, which is addressed in research dealing with improved synthesis methods [19, 20]. The reason for the decreased bulk conductivity is not yet understood.

In the following, we denote the Al occupation rate by the number of Al ions per hexagonal unit cell n_{Al} . In the case of charge compensation by Li, the composition index x , introduced in Equation (1), is equal to $n_{\text{Al}}/6$. For the purpose of our simulations, we however decouple n_{Al} from the number of Li ions per cell, n_{Li} , unless denoted otherwise.

2.2. Computational details

The DFT calculations presented in this work were performed using the Quantum ESPRESSO (QE) PWscf and NEB routines [21, 22]. We used the ultrasoft Garrity-Bennet-Rabe-Vanderbilt (GBRV) pseudopotentials [23], a plane wave basis with a cutoff energy of 40 Ry, and the generalized gradient approximation (GGA) of the exchange-correlation functional by Perdew *et al.* (PBE) [24]. Brillouin zone integrations were carried out on a Γ -centered grid of $6 \times 6 \times 2$ k -points following the scheme of Monkhorst and Pack [25]. Unless specified otherwise, each calculation was performed allowing for ionic relaxation using the Broyden-Fletcher-Goldfarb-Shanno (BFGS) algorithm implemented in the QE routines. Cell volume relaxations were carried out at fixed unit cell symmetry. Energy profiles and barriers were determined using the nudged elastic band (NEB) and climbing image (CI) methods [26]. Sets of symmetrically inequivalent ionic configurations were constructed using the site-occupation disorder (SOD) code of Grau-Crespo *et al.* [27]. Crystal structures were visualized with VESTA [28].

3. Results

3.1. Dependence of structural parameters and Li interstitial formation on Al content

3.1.1. Cell parameters In order to examine the influence of the Al content in LATP on the cell parameters, we performed DFT calculations allowing ionic relaxation and optimization of lattice vectors for various configurations of the Ti/Al occupancy. Considering every possible occupation of the 12 Al/Ti sites in the LATP supercell (*cf.* Figure 1) by a combination of these elements yields in total 236 symmetrically inequivalent configurations. For $n_{\text{Al}} \in \{0, 1, 11, 12\}$, there is only a single structure which

needs to be considered. For $n_{\text{Al}} \in \{2, 3, 10\}$, we considered the full set of symmetrically inequivalent configurations, namely 9, 19 and 9, respectively. For $n_{\text{Al}} \in \{4, 5, 6, 7, 8, 9\}$, there are $\{50, 66, 90, 66, 50, 19\}$ configurations, respectively, out of which we randomly chose six each for further analysis. Independent of n_{Al} , the number of Li ions was kept constant at $n_{\text{Li}} = 6$.

Figure 2 shows the resulting lattice parameters a and c corresponding to the cell dimensions in $\langle 01\bar{1}0 \rangle$ and $\langle 0001 \rangle$ directions, respectively. The cell parameter a shows a linear decrease with the number of Al ions, closely following the empirical Vegard rule. For c , the deviation from the Vegard rule is more apparent, and individual configurations at the same n_{Al} show a noticeable spread. Upon increasing the Al content to its maximum, a and c decrease by 1.8% and 1.4%, respectively. This leads to an increasing ratio c/a with n_{Al} , implying an anisotropic cell volume change, as the cell contracts stronger in the $\{0001\}$ planes than along the $\langle 0001 \rangle$ directions.

3.1.2. Polyhedra To further investigate the anisotropic change of the lattice parameters with n_{Al} , we analyzed the variation in the volumes of the polyhedral substructures. To this end, the volumes of the oxygen polyhedra surrounding the cations were calculated for all examined configurations with $n_{\text{Al}} = 6$. Large differences between the polyhedra are observed, as visualized in the inset of Figure 2. While the small P tetrahedra show only little fluctuations, the fluctuations become noticeably larger for the Ti and Al octahedra, and the volumes of the Li(M1) octahedra vary the most.

3.1.3. M1/2 pair occupation In order to analyze the influence of the ionic structure on Li migration, we first considered a single Li M1/2 pair ($n_{\text{Li}} = 7$) and a single Al ion ($n_{\text{Al}} = 1$) in our LATP supercell model. We calculated the total energies of all possible inequivalent configurations of this setup by relaxing the ionic positions while keeping the cell dimensions fixed at the values $a = 8.63 \text{ \AA}$ and $c = 21.13 \text{ \AA}$, obtained in Section 3.1.1 for $n_{\text{Al}} = 1$. The resulting energies are plotted in Figure 3 with respect to the distance between the Al ion and the M1/2 pair. As a measure of the M1/2 pair position, we chose the mean of the position vectors of the two constituting Li ions. Energy differences of up to 0.32 eV can be observed, and the non-uniform energy-distance relationship indicates anisotropic interaction between the Al ion and the Li M1/2 pair. Additionally, we calculated the inverse distances between the 2 Li ions on the opposing M1/2 positions, which are also plotted in Figure 3. These distances show a behavior similar to the energy, suggesting a significant contribution of M1/2-M1/2 Coulomb repulsion to the interaction energy.

As a brief summary of Section 3.1, it is observed that the variation of the Al occupation leads to cell volume changes in agreement with the Vegard rule. The polyhedra around a given ion type in a given composition vary in size. Furthermore, it is seen that the total energy of the Li M1/2 pair is sensitive to its relative position with respect to a nearby Al ion.

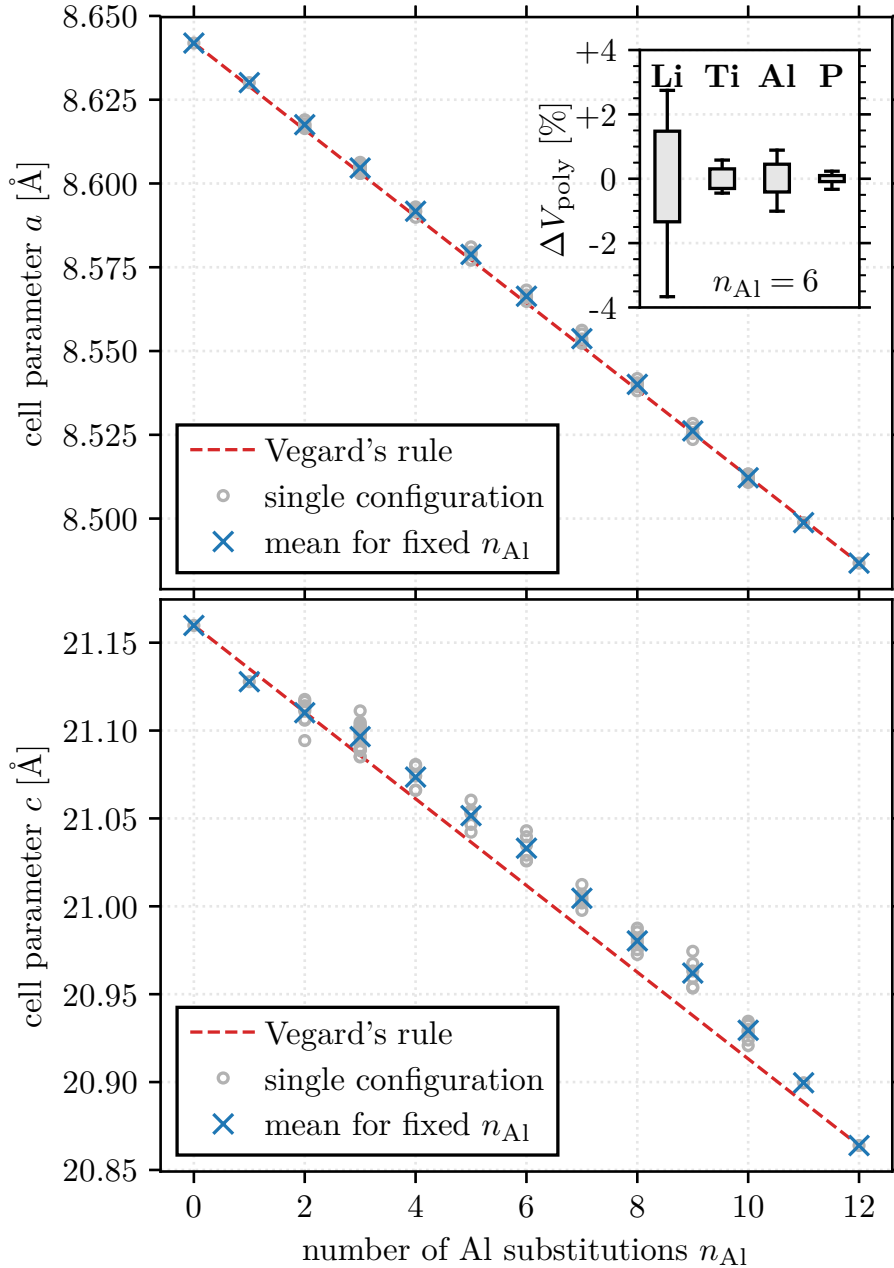


Figure 2. (Color online) Crystal lattice parameters of LATP as a function of the Al content. Upper panel: lattice parameter a , i.e. the length of the cell vector in $\langle 01\bar{1}0 \rangle$ direction. Lower panel: lattice parameter c , i.e. the length of the cell vector in $\langle 0001 \rangle$ direction. The values obtained for the individual ionic configurations on the Al/Ti sublattice (gray circles) are averaged (blue crosses) for each number of Al ions in the simulation cell. Dashed red lines indicate a linear decrease as expected from Vegard's rule. In the inset, relative fluctuations of polyhedral volumes are visualized for the case of $n_{\text{Al}} = 6$. For each element, the box represents the spread of all polyhedron volumes for all calculated cell configurations, relative to the mean of the element's data set. The vertical extent of the boxes encompass the 50% of data points closest to the respective means, and the capped lines illustrate the most extreme volumes that occurred.

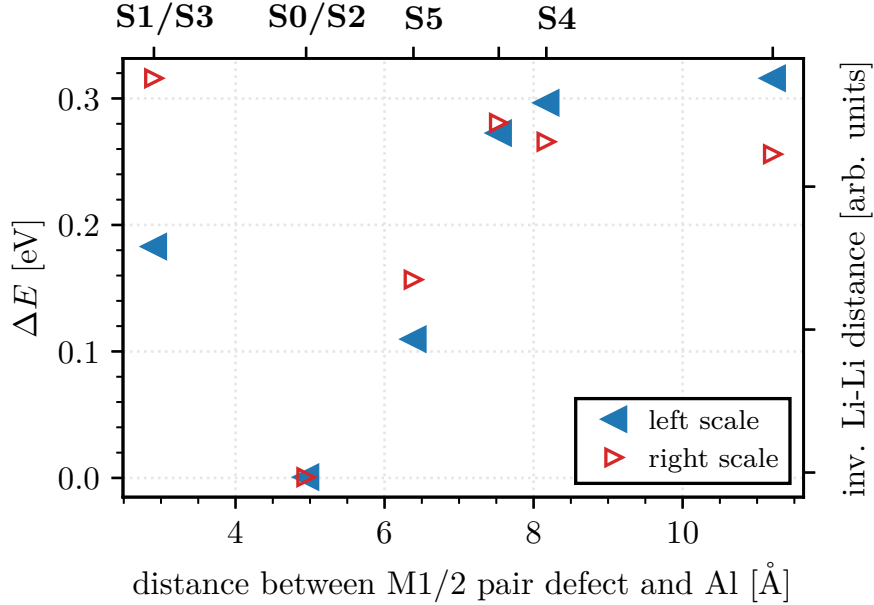


Figure 3. (Color online) Interaction between a Li M1/2 pair and a nearby Al ion. Filled, blue triangles pointing left: Energy (ΔE) of one Li M1/2 pair in an LATP unit cell with $n_{\text{Al}} = 1$, with respect to the lowest energy of this data set, as a function of the distance to the closest Al ion. The position of the M1/2 pair is chosen as the geometric mean of the positions of its two constituting Li ions. Open, red triangles pointing right: Inverse distance between the two Li ions of the M1/2 pair given in arbitrary units. Periodic boundary conditions are considered for all distance calculations. The labels on the upper horizontal axis relate the (M1/2-M1/2)-Al distances to the sites occupied by Al as visualized in Figure 1 (bottom panel), given that the M1/2 pair is located between S0-S1-S2-S3.

3.2. Influence of nearby Al ions on the Li migration energy profiles

With the calculations presented in this section, we examine the effect of Al on the migration energy landscape of Li M1/2 pairs. To this end, we consider a set of four Al/Ti sites in the vicinity of the Li migration path, namely the sites S1, S2, S3 and S4, as displayed in Figure 1, and vary their occupations. With all other sites in the cell being occupied by Ti, the resulting 10 symmetrically inequivalent configurations can be categorized into 4 symmetric configurations and 6 asymmetric configurations: The former are point symmetric around the M2 site with respect to their Ti and Al occupations, while the latter are not. For each of the 10 configurations, the energy profile between initial and final state of the interstitial mechanism (*cf.* Section 2.1) was calculated with the NEB method. Again, only one Li M1/2 pair was placed in the cell ($n_{\text{Li}} = 7$). The cell parameters a and c were chosen according to the mean values of the respective Al contents n_{Al} , as derived in Section 3.1. They were kept constant during the NEB calculations. For the calculations of the asymmetric configurations, 11 NEB images were used between initial and final state. For the symmetric configurations, only the

first half of the path needs to be examined, as the other half is symmetrically identical. In this case, 7 intermediary images were calculated between initial and M2 transition state. For both sets, the climbing image (CI) method was applied to accurately sample the saddle point energy.

To analyze the data, we introduce a naming scheme addressing the occupational configurations and their corresponding energy profile by a string of four letters. It is constructed by taking the first letter of the elements occupying the Ti/Al sites (i.e. A for Al and T for Ti) in the order S1, S2, S3, S4 as enumerated in [Figure 1](#). In this way, symmetry and neighborhood relations are intuitively visible: A symmetric name corresponds to a symmetric energy profile (e.g. ATTA). Names that are mirrored versions of each other indicate equivalent configurations (e.g. ATAA and AATA), and the first (last) three letters denote the occupations surrounding one (the other) M1 site. The letters x and y denote arbitrary Ti/Al occupations, and names containing x and y reference the set of possible configurations.

The energy profiles of the symmetric configurations, with respect to the energy of their initial states, are presented in the top panel of [Figure 4](#). A clear distinction between two different profile types is apparent: The two paths with Ti closest to the M2 position, TTTT and ATTA, yield quite similar energy profiles along the migration path, with an energy barrier of around 0.18 eV. The M2 transition state is a global energy maximum for TTTT, and a local one for ATTA. The main difference of the two curves is the presence of an energy maximum between initial state and transition state for ATTA, in contrast to the TTTT curve, which increases monotonically in this interval. The curves for TAAT and AAAA differ significantly from those for TTTT and ATTA, both in height and shape. Most notably, their energy barriers are reduced by about 0.1 eV, to 0.07 eV (TAAT) and 0.09 eV (AAAA). Moreover, the M2 transition state is a local energy minimum surrounded by two maxima.

The profiles of the asymmetric paths ([Figure 4](#), central panel) are more diverse at first sight. The energy differences between initial and final state vary at a scale of the order of the barriers themselves. They are in agreement with the Li M1/2 pair formation energies shown in [Figure 3](#). For example, the initial state of configuration TATT has an Al occupation on an S2 type site. The final state of the same configuration, equivalent to the initial state of TTAT, has an S3 site occupied by Al. Both in [Figure 3](#) and [Figure 4](#), one finds an energy difference of about 0.18 eV between these states.

Despite the energy differences between initial and final states, the shapes of the asymmetric curves show similarities to the symmetric ones. For a better comparability, we remove the tilt in the curves by subtracting a constant gradient. This corresponds to a decomposition of the energy profile along the reaction coordinate, $E(z)$, into a slope term $E_{\text{slope}}(z) \propto z$ and a shape term $E_{\text{shape}}(z)$:

$$\begin{aligned} E(z) &= E_{\text{slope}}(z) + E_{\text{shape}}(z) \\ &= [E(1) - E(0)] \cdot z + E_{\text{shape}}(z). \end{aligned} \tag{2}$$

The resulting functions $E_{\text{shape}}(z)$ are depicted in the lower panel of [Figure 4](#), together

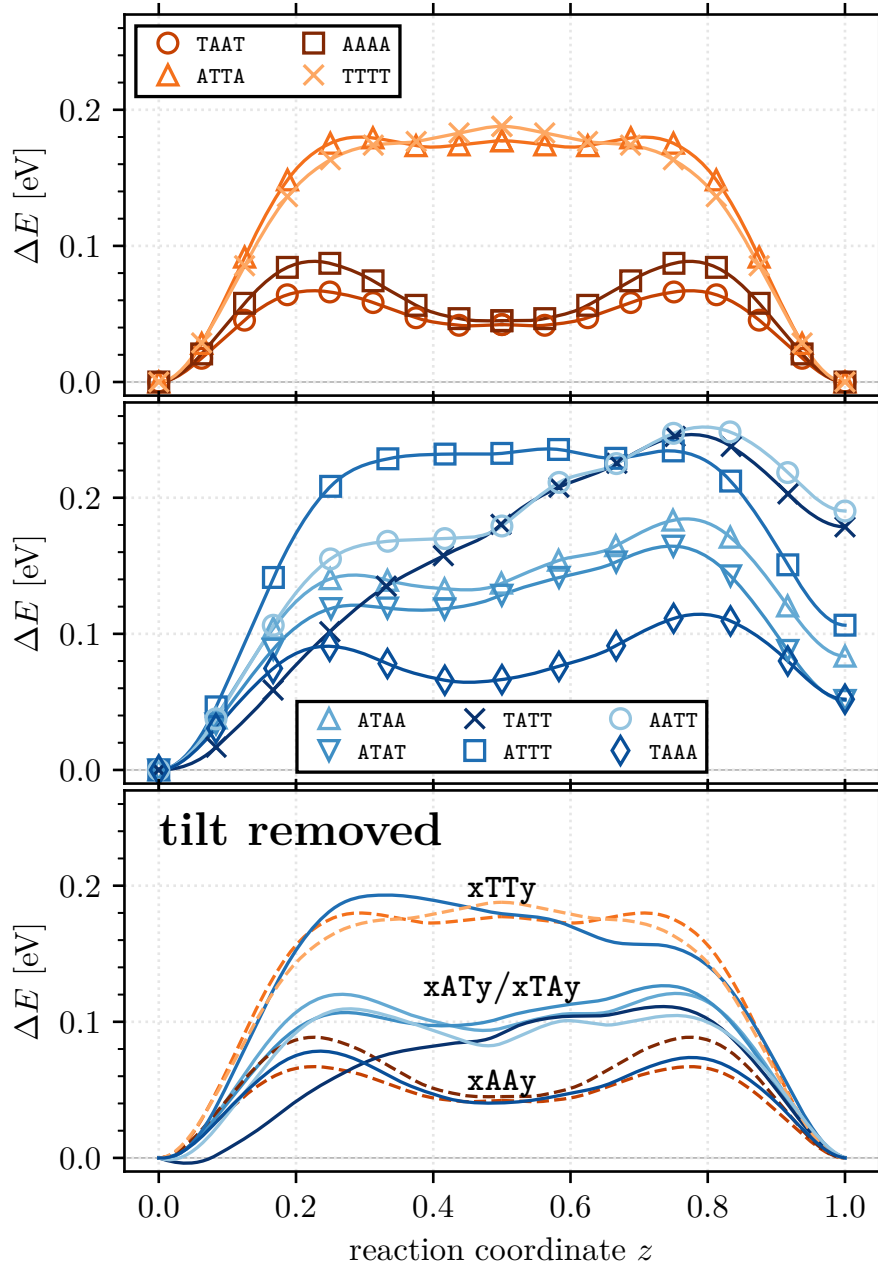


Figure 4. (Color online) Energy profiles of the interstitial migration paths in LATP, from initial ($z = 0$) to final state ($z = 1$), with respect to the energy of the former, for various neighboring Ti/Al-configurations. The top panel shows the symmetric profiles, i.e. those where initial and final state are identical, and the central panel shows the asymmetric profiles. The corresponding configurations are named as defined in Section 3.2. Subtracting the energy slope between initial and final state yields the shapes displayed in the bottom panel, where dashed and continuous lines represent symmetric and asymmetric profiles, respectively.

with the symmetric curves for comparison. A split into three distinct types is observed: asymmetric profiles corresponding to paths where the Al/Ti positions neighboring the M2 site (types S2 and S3, *cf.* Figure 1) are both occupied by Ti or both occupied by Al, fall into the same categories as the respective symmetric profiles. The set \mathbf{xAAy} is characterized by a low barrier and a local minimum, and the set \mathbf{xTTy} by a higher barrier and an energy plateau around the M2 transition state. The other set of paths, \mathbf{xATy} and \mathbf{xTAY} , forms a category of its own, with intermediate barriers.

As a brief summary of Section 3.2, the calculated profiles show a great variance in their energy barriers and energy differences between initial and final states, hinting at a quite heterogeneous energy landscape for the migration of Li M1/2 pairs. However, the energy profiles have characteristic shapes, dictated by the Al/Ti occupation of the sites closest to the M2 site, allowing the determination of three distinct categories.

3.3. Influence of the cell volume on migration energy profiles

In the previous section, we examined the influence of local Al occupations within the unit cell on the migration path profiles. With a final set of calculations, we now investigate two further aspects: Primarily, we intend to decouple the chemical, electronic influence of nearby Al/Ti occupations from a purely geometrical one, caused by a deformation of the network of interconnected polyhedra (*cf.* Figure 1). Secondly, we aim to estimate the long-range influences of Al occupations, conveyed through such mechanical deformations.

Both of these problems can be tackled simultaneously by analyzing the influence of the unit cell volume on the energy profiles. In order to compare the different behavior caused by either a Ti or an Al occupation, we examine the two limiting cases: (i) pure LTP (no Al ions, $n_{\text{Al}} = 0$) and (ii) the fully substituted simulation cell (all Ti ions replaced by Al, $n_{\text{Al}} = 12$, ‘‘LAP’’). In both cases we consider one Li M1/2 pair occupation (*i.e.* $n_{\text{Li}} = 7$). We carried out seven NEB migration path calculations for each of the two compounds, each at a constant, different volume. These volumes were determined by the cell parameters (a, c) corresponding to their mean values for $n_{\text{Al}} \in \{0, 2, 4, 6, 8, 10, 12\}$ as obtained in Section 3.1. As the paths are symmetrical for both compounds, the energy landscapes are computed between initial and transition state only, and discretized by five intermediary images. The resulting profiles are depicted in Figure 5.

In the case of LTP, a clear transition between profile shapes is visible. For large volumes (corresponding *e.g.* to a small average n_{Al} in an extended material), the shapes are in agreement with those of type \mathbf{xTTy} discussed in Section 3.2: There is an energy plateau in the proximity of the transition state, which is a global maximum or a very flat minimum. For decreasing cell volumes (corresponding *e.g.* to larger average n_{Al} values in an extended material) the transition state energy decreases and the intermediate maximum increases relative to the initial state energy, making the minimum of the transition state more pronounced. The overall energy barrier remains similar for all volumes. For the profiles at full Al occupation (LAP), a similar trend is visible at small volumes ($n_{\text{Al}} > 7$). However, for larger volumes corresponding to $n_{\text{Al}} \leq 6$, the

intermediate energy maximum vanishes, and the relative transition state energy also lowers at a similar rate, resulting in a monotonic energy increase between initial and transition state at large volumes.

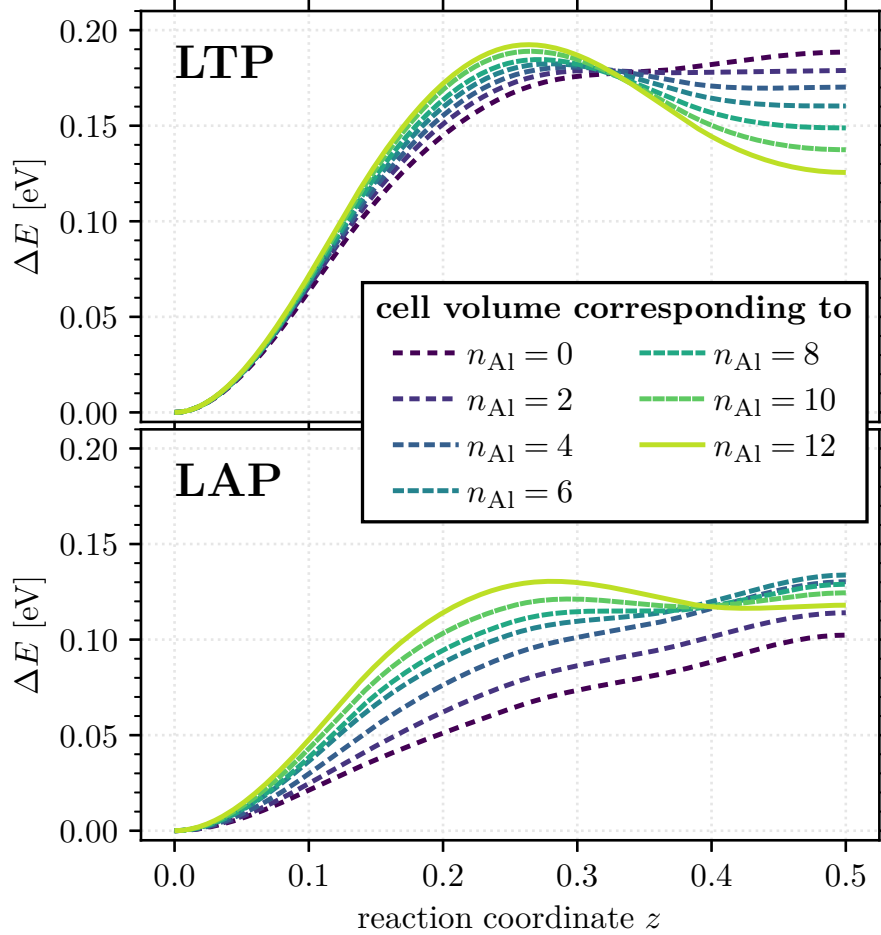


Figure 5. (Color online) Energy profiles of the interstitial migration path between initial ($z = 0$) and M2 transition state ($z = 0.5$) as a function of the cell volume for LTP (upper panel) and LAP (lower panel). The different curves were obtained by varying the cell volume. Therefore, the lattice parameters were chosen according to their averaged values at fixed Al content n_{Al} (*cf.* legend) as obtained in Section 3.1. Darker line shades and wider separation of dashes indicate larger volumes.

4. Discussion

In this section, we discuss the results presented in Sections 3.1 to 3.3 dealing with the different aspects of varying the Al/Ti occupation in LATP, which concern the crystal structure and the migration properties of Li.

In Section 3.1, we described an anisotropic contraction of the LATP cell with increasing Al content and a fixed number of Li ions: With a relative change of -1.4%

when going from LTP to LAP, the lattice parameter c turned out to be less affected by the Al/Ti occupations compared to the lattice parameter a , which exhibits a relative decrease of -1.8% . This yields an increase of the c/a ratio by $+0.4\%$ between LTP and LAP. Individually, a and c shrink with increasing Al content following Vegard’s rule, since six-fold coordinated Ti(4+) ions have an ionic radius of 0.61 \AA compared to 0.54 \AA of Al(3+) in the same configuration [29]. The different influence on a and c can be explained by the changes of oxygen polyhedron volumes described in Section 3.1 (*cf.* inset in Figure 2): The polyhedra around Al, Ti and P are quite rigid due to the relatively high number of valence electrons of these elements, leading to strong bonds with the surrounding oxygen ions. Therefore, these polyhedra propagate local volume changes induced by introducing additional Al easily, by pushing and pulling neighboring polyhedra. The Li-M1-octahedra, however, are much more flexible, due to only a single valence electron of Li bonding with six oxygen ions. As the Al/Ti octahedra and the Li(M1) octahedra are aligned in [0001]-direction, the latter effectively act as a buffer, compensating local volume changes due to varying Al/Ti occupations by expansion and contraction in [0001]-direction, thereby lowering the impact on the overall c parameter. This behavior was also described for LTP compounds with full substitutions on the Ti and P lattices [18]. Experimental data for LATP with $0 \leq x \leq 0.5$ (*cf.* Equation (1)) measured by Redhammer *et al.* [30] show an opposite trend: While a decreases similarly to our results, c shrinks notably more, resulting in a decreasing c/a ratio with increasing x . In this case, however, the number of Li ions also changes with x , leading to a growing number of paired M1/2 site occupations, which were not considered in our calculations. Each of these occupations replaces one flexible Li(M1) octahedron by two stiffer Li(M1/2) tetrahedra, with stronger bonds between Li and O. Consequently, the overall buffering effect is weakened up to the point where the c/a ratio decreases with x , which explains the discrepancy between the experimental data and our presented results. Nevertheless, the absolute volume change of the cell is rather small in both cases, implying high mechanical stability. Note that the cell parameters presented in this research systematically overestimate the experimental values by about 1.5% , as typically observed in DFT calculations using the PBE functional.

The nontrivial relationship between the energy of a Li M1/2 pair and its distance to the closest Al ion shown in Figure 3 can also be attributed to the large influence of structural effects in LATP. Direct Coulombic repulsion of the paired Li ions on M1/2 sites has a considerable impact on the formation energy of the pair, as its correlation with the inverse M1/2-M1/2 distance suggests. This distance is influenced by the position of the Al ion relative to the Li pair. In order to illustrate these relationships, we consider one M1/2 pair surrounded by the sites S0-S1-S2-S3 as defined in Figure 1. Substitution of Ti by Al on an S0 (S2) site reduces the respective octahedron volume, pulling the M1/2 ions apart, which results in a reduction of the potential energy. Substitution of Ti by Al on the S5 position has a weaker influence, since it only indirectly acts on the M1/2 pair distance by increasing the space between neighboring lanterns. The more the Al ion and the M1/2 pair are separated, the smaller is the effect of the octahedron

volume reduction on the M1/2 pair distance. The M1/2 pair distance vector is largely aligned in the (0001) plane, i.e. it only has a comparatively small component in [0001] direction. Consequently, a volume reduction of octahedra aligned in [0001]-direction, as e.g. induced by substitution of Ti by Al on an S1 (S3) site, effectively decreases the pair distance. This effect, which is strongest for an M1/2 pair directly adjacent to Al, leads to an increase of the potential energy. Coulomb repulsion between Li ions was reported by He *et al.* [14] to have a major influence on Li pair mobility in super-ionic conductors. Our findings of a correlation between M1/2 pair energy and inverse Li distance qualitatively support this statement, since the migration energy landscape, which essentially affects the ionic mobility, is to a large extent determined by the site energies of the migrating species. The considerable energy differences between differently surrounded M1/2 pair occupations of up to 0.32 eV, being of the order of the migration barriers, hint at a significant reduction of M1/2 mobility, as will be discussed in more detail below. Note however, that the calculated energy differences are likely to be overestimated: Due to the finite size limitations of the simulation cell considered in this study, the interactions between occupations in neighboring periodic cells are stronger in the (0001)-plane than in the [0001] direction, since $a < c$. For larger simulation cells, one should expect a clearer convergence of the formation energies with distance for the long-range interactions.

The migration profiles presented in Section 3.2 exhibit considerable variance in shape and height, implying a diverse energy landscape for interstitial Li migration within LATP. In this regard, our research supports the assumption of Epp *et al.* [13] of a heterogeneous diffusion landscape based on measurements of Li diffusion activation energies. This also offers a possible explanation for the reported sensitivity of LATP bulk ionic conductivity to the synthesis parameters [7], as an inhomogeneous spread of Al occupations could notably influence the overall connectivity of Li sites in the network.

While Lang *et al.* [12] reported a significant energy difference between the M1/2 pair occupation and the M2 transition state, recent calculations by Zhang *et al.* [16] suggest that these states should be nearly equal in energy. Our results cannot support the latter, but rather are consistent with the former observation.

The classification of the energy profiles into three categories shows the importance of the Al/Ti-occupation of the sites directly adjacent to the octahedron around the M2 position (sites S2 and S3 in Figure 1) for the Li pathway. An increased Al occupation of these sites results in more favorable, i.e. lower, migration barriers. While the M2 transition state thereby tends to be stabilized, the large energy slopes, and the M1/2 rotational barriers which are not investigated here, remain potentially significant obstacles for long-range Li diffusion. The importance of Al/Ti sites on the same (0001)-plane as the M1/2 pair occupation for the energetics, as discussed above, suggests that considering a larger environment of Al/Ti sites around the migration path may reveal an even finer categorization.

The calculations at varied cell parameters described in Section 3.3 show a transition between single-peak and double-peak energy profiles for Li migration as a function of

the cell volume. It is therefore reasonable to assume that the change in profile shapes described in Section 3.2 can to some extent be attributed to the geometrical effect of a changed cell volume. As the double-peak occurs when a Li ion crosses the polyhedral face of the M2 cavity, Li-O interactions are likely to be responsible for this characteristic shape.

5. Conclusion

In this study, we analyzed the effect of the Al content and the ionic distribution on the Al/Ti sublattice on the structure and Li ion migration properties of LATP super-ionic conductors. A mechanical picture of interlinked oxygen polyhedra, and their flexibility with respect to local geometrical changes, provides qualitative insights into the system's reaction to varying Al content and internal volume changes. Energy profiles for interstitial migration of Li M1/2 pairs can be categorized into three basic shapes apart from an overall energy slope. The characteristic profile shapes belonging to the different categories were shown to depend on the overall volume of the system, and the most favourable migration path occurs when two Al polyhedra are adjacent to the M2 cavity. The formation energies of Li M1/2 pairs, which determine the energy slopes between initial and final states of Li migration, vary on the scale of the barrier energies depending on their local ionic environment. These formation energies were found to strongly depend on the configuration of the surrounding Al/Ti site occupations, which defines the Li-Li distance of the M1/2 pair. A complete picture of the total influence of Al on the ionic conductivity of LATP requires the consideration of additional effects such as the existence of rotational barriers of M1/2 pairs, as well as the interactions between individual M1/2 pair occupations. However, the data presented in this paper serves as a solid basis to study Li diffusion in LATP on a larger scale using simplified models, e.g. by performing Kinetic Lattice Monte Carlo simulations for a network of Li sites in LATP with varying Al/Ti composition.

Acknowledgments

This work was funded by the German Research Foundation (DFG), Grant No. El 155/26-1. The calculations were carried out on the computing facility ForHLR I of the Steinbuch Centre for Computing (SCC) of the Karlsruhe Institute of Technology (KIT), funded by the Ministry of Science, Research, and Arts Baden-Württemberg, Germany, and by the DFG.

References

- [1] Tarascon J M and Armand M 2001 *Nature* **414** 359–367 URL <https://doi.org/10.1038/35104644>
- [2] Li J, Ma C, Chi M, Liang C and Dudney N J 2014 *Advanced Energy Materials* **5** 1401408 URL <https://doi.org/10.1002/aenm.201401408>

- [3] Fan L, Wei S, Li S, Li Q and Lu Y 2018 *Advanced Energy Materials* **8** 1702657 URL <https://doi.org/10.1002/aenm.201702657>
- [4] Zheng F, Kotobuki M, Song S, Lai M O and Lu L 2018 *Journal of Power Sources* **389** 198–213 URL <https://doi.org/10.1016/j.jpowsour.2018.04.022>
- [5] Aono H 1990 *Journal of The Electrochemical Society* **137** 1023 URL <https://doi.org/10.1149/1.2086597>
- [6] Rossbach A, Tietz F and Grieshammer S 2018 *Journal of Power Sources* **391** 1–9 URL <https://doi.org/10.1016/j.jpowsour.2018.04.059>
- [7] Breuer S, Prutsch D, Ma Q, Epp V, Preishuber-Pflügl F, Tietz F and Wilkening M 2015 *Journal of Materials Chemistry A* **3** 21343–21350 URL <https://doi.org/10.1039/c5ta06379e>
- [8] Arbi K, Hoelzel M, Kuhn A, García-Alvarado F and Sanz J 2013 *Inorganic Chemistry* **52** 9290–9296 URL <https://doi.org/10.1021/ic400577v>
- [9] Arbi K, Jimenez R, Šalkus T, Orliukas A and Sanz J 2015 *Solid State Ionics* **271** 28–33 URL <https://doi.org/10.1016/j.ssi.2014.10.016>
- [10] Monchak M, Hupfer T, Senyshyn A, Boysen H, Chernyshov D, Hansen T, Schell K G, Bucharsky E C, Hoffmann M J and Ehrenberg H 2016 *Inorganic Chemistry* **55** 2941–2945 URL <https://doi.org/10.1021/acs.inorgchem.5b02821>
- [11] Case D, McSloy A J, Sharpe R, Yeandel S R, Bartlett T, Cookson J, Dashjav E, Tietz F, Kumar C N and Goddard P 2020 *Solid State Ionics* **346** 115192 URL <https://doi.org/10.1016/j.ssi.2019.115192>
- [12] Lang B, Ziebarth B and Elsässer C 2015 *Chemistry of Materials* **27** 5040–5048 URL <https://doi.org/10.1021/acs.chemmater.5b01582>
- [13] Epp V, Ma Q, Hammer E M, Tietz F and Wilkening M 2015 *Physical Chemistry Chemical Physics* **17** 32115–32121 URL <https://doi.org/10.1039/c5cp05337d>
- [14] He X, Zhu Y and Mo Y 2017 *Nature Communications* **8** URL <https://doi.org/10.1038/ncomms15893>
- [15] Kuo P H and Du J 2019 *The Journal of Physical Chemistry C* **123** 27385–27398 URL <https://doi.org/10.1021/acs.jpcc.9b08390>
- [16] Zhang B, Lin Z, Dong H, Wang L W and Pan F 2020 *Journal of Materials Chemistry A* **8** 342–348 URL <https://doi.org/10.1039/c9ta09770h>
- [17] Hagman L O, Kierkegaard P, Karvonen P, Virtanen A I and Paasivirta J 1968 *Acta Chemica Scandinavica* **22** 1822–1832 URL <https://doi.org/10.3891/acta.chem.scand.22-1822>
- [18] Mutter D, Urban D F and Elsässer C 2019 *Journal of Applied Physics* **125** 215115 URL <https://doi.org/10.1063/1.5091969>
- [19] Bucharsky E, Schell K, Hintennach A and Hoffmann M 2015 *Solid State Ionics* **274** 77–82 URL <https://doi.org/10.1016/j.ssi.2015.03.009>
- [20] Bucharsky E C, Schell K G, Hupfer T, Hoffmann M J, Rohde M and Seifert H J 2016 *Ionics* **22** 1043–1049 URL <https://doi.org/10.1007/s11581-015-1628-3>
- [21] Giannozzi P, Baroni S, Bonini N, Calandra M, Car R, Cavazzoni C, Ceresoli D, Chiarotti G L, Cococcioni M, Dabo I, Dal Corso A, de Gironcoli S, Fabris S, Fratesi G, Gebauer R, Gerstmann U, Gougoussis C, Kokalj A, Lazzeri M, Martin-Samos L, Marzari N, Mauri F, Mazzarello R, Paolini S, Pasquarello A, Paulatto L, Sbraccia C, Scandolo S, Sclauzero G, Seitsonen A P, Smogunov A, Umari P and Wentzcovitch R M 2009 *Journal of Physics: Condensed Matter* **21** 395502 (19pp) URL <http://www.quantum-espresso.org>
- [22] Giannozzi P, Andreussi O, Brumme T, Bunau O, Nardelli M B, Calandra M, Car R, Cavazzoni C, Ceresoli D, Cococcioni M, Colonna N, Carnimeo I, Corso A D, de Gironcoli S, Delugas P, Jr R A D, Ferretti A, Floris A, Fratesi G, Fugallo G, Gebauer R, Gerstmann U, Giustino F, Gorni T, Jia J, Kawamura M, Ko H Y, Kokalj A, Küçükbenli E, Lazzeri M, Marsili M, Marzari N, Mauri F, Nguyen N L, Nguyen H V, de-la Roza A O, Paulatto L, Poncé S, Rocca D, Sabatini R, Santra B, Schlipf M, Seitsonen A P, Smogunov A, Timrov I, Thonhauser T, Umari P, Vast N, Wu X and Baroni S 2017 *Journal of Physics: Condensed Matter* **29** 465901 URL

- <https://doi.org/10.1088%2F1361-648x%2Faa8f79>
- [23] Garrity K F, Bennett J W, Rabe K M and Vanderbilt D 2014 *Computational Materials Science* **81** 446–452 URL <https://doi.org/10.1016/j.commatsci.2013.08.053>
- [24] Perdew J P, Burke K and Ernzerhof M 1997 *Physical Review Letters* **78** 1396–1396 URL <https://doi.org/10.1103/physrevlett.78.1396>
- [25] Monkhorst H J and Pack J D 1976 *Physical Review B* **13** 5188–5192 URL <https://doi.org/10.1103/physrevb.13.5188>
- [26] Henkelman G, Uberuaga B P and Jónsson H 2000 *The Journal of Chemical Physics* **113** 9901–9904 URL <https://doi.org/10.1063/1.1329672>
- [27] Grau-Crespo R, Hamad S, Catlow C R A and de Leeuw N H 2007 *Journal of Physics: Condensed Matter* **19** 256201 URL <https://doi.org/10.1088%2F0953-8984%2F19%2F25%2F256201>
- [28] Momma K and Izumi F 2011 *Journal of Applied Crystallography* **44** 1272–1276 URL <https://doi.org/10.1107/S0021889811038970>
- [29] Shannon R D 1976 *Acta Crystallographica Section A* **32** 751–767 (Preprint <https://onlinelibrary.wiley.com/doi/pdf/10.1107/S0567739476001551>) URL <https://doi.org/10.1107/S0567739476001551>
- [30] Redhammer G, Rettenwander D, Pristat S, Dashjav E, Kumar C, Topa D and Tietz F 2016 *Solid State Sciences* **60** 99–107 URL <https://doi.org/10.1016/j.solidstatesciences.2016.08.011>
- [31] Anantharamulu N, Rao K K, Rambabu G, Kumar B V, Radha V and Vithal M 2011 *Journal of Materials Science* **46** 2821–2837 URL <https://doi.org/10.1007/s10853-011-5302-5>
- [32] Arbi K, Mandal S, Rojo J M and Sanz J 2002 *Chemistry of Materials* **14** 1091–1097 URL <https://doi.org/10.1021/cm010528i>
- [33] Arbi K, Hoelzel M, Kuhn A, García-Alvarado F and Sanz J 2014 *Phys. Chem. Chem. Phys.* **16** 18397–18405 URL <https://doi.org/10.1039/c4cp02938k>
- [34] Bachman J C, Muy S, Grimaud A, Chang H H, Pour N, Lux S F, Paschos O, Maglia F, Lupart S, Lamp P, Giordano L and Shao-Horn Y 2015 *Chemical Reviews* **116** 140–162 URL <https://doi.org/10.1021/acs.chemrev.5b00563>
- [35] Hayamizu K and Seki S 2017 *Physical Chemistry Chemical Physics* **19** 23483–23491 URL <https://doi.org/10.1039/c7cp03647g>
- [36] Hupfer T, Bucharsky E C, Schell K G, Senyshyn A, Monchak M, Hoffmann M J and Ehrenberg H 2016 *Solid State Ionics* **288** 235–239 URL <https://doi.org/10.1016/j.ssi.2016.01.036>
- [37] Jian Z, Hu Y S, Ji X and Chen W 2017 *Advanced Materials* **29** 1601925 URL <https://doi.org/10.1002/adma.201601925>
- [38] Kotobuki M and Koishi M 2013 *Ceramics International* **39** 4645–4649 URL <https://doi.org/10.1016/j.ceramint.2012.10.206>
- [39] Pan H, Hu Y S and Chen L 2013 *Energy & Environmental Science* **6** 2338 URL <https://doi.org/10.1039/c3ee40847g>
- [40] Pérez-Estébanez M, Isasi-Marín J, Töbrens D, Rivera-Calzada A and León C 2014 *Solid State Ionics* **266** 1–8 URL <https://doi.org/10.1016/j.ssi.2014.07.018>
- [41] Xu M, Ding J and Ma E 2012 *Applied Physics Letters* **101** 031901 URL <https://doi.org/10.1063/1.4737397>
- [42] Zhang B, Tan R, Yang L, Zheng J, Zhang K, Mo S, Lin Z and Pan F 2018 *Energy Storage Materials* **10** 139–159 URL <https://doi.org/10.1016/j.ensm.2017.08.015>